3. Geophysical Fluid Dynamics

Experimental study on the three dimensional spherical convections with the parameters of planetary atmospheres

Contact Person: Yoshi-Yuki Hayashi
Graduate School of Mathematical Sciences
University of Tokyo

Research Organization: Yoshi-Yuki Hayashi
Shin-ichi Takehiro[1]
Masaki Ishiwatari[2], Masahiro Hosaka[3]
Geophysical Fluid Dynamics Group,
Graduate School of Mathematical Sciences, University of Tokyo

Keywords: spherical convection, general circulation, planetary atmospheres, angular momentum, zonal mean flow, teleconnection patterns, SST anomaly, heating response

1. Background

The grand purpose of our study is to reveal the dynamical structures which underlie the general circulations of the planetary atmospheres. It is aimed to construct a theoretical framework which is useful in describing their circulation characteristics, as tried by Golitsyn[1] since 1960's. Our interest in due course is to recognize the atmosphere of the earth (or the climate of the earth) as one of the possible realizations in the physical parameter space observed in the solar system.

One of our procedures in revealing the possible underlying dynamics is to gather and classify atmospheric circulation patterns which might be observed under various values of planetary "external" conditions such as orbital parameters (amount and variation of the incoming solar flux), radius and rotation rate of the planet, radiation property of the atmosphere, and surface boundary setups. The sampling of the possible atmospheric circulations may be possible by numerical experiments by the use of the super computer powers.

Our search in circulation patterns is now performed for the following three major targets:

1. to reveal the possible circulations which might be realized with the values of solar flux and orbital parameters which are related to Mars, Earth and Venus,
2. to reveal the possible circulations which might be realized with the earth's condition, but with strongly simplified surface and/or physical processes,
3. to reveal the possible circulations which might be realized as convection of a spherical shell in general.

These are the targets being studied continuously from the preceding years.

[1] Present affiliation: Faculty of Science, Kyushu University

[2] Present affiliation: Graduate School of Environmental Earth Science, Hokkaido University

[3] Present affiliation: Climate Research Department, Meteorological Research Institute, Japan Meteorological Agency

The first target is the three dimensional calculations of the so called runaway greenhouse effect. It has been argued, in relation to the evolution of the atmospheres of Venus, Earth and Mars, that there exists a limit of radiation which can be emitted from the top of the atmosphere with the ocean[5]. The interesting point is that the radiation limit predicted in the literature is not far from the value of the incoming solar flux of the present earth. It is about 300 W/m^2. The argument placed so far is presented by the use of one dimensional models. It is of interest to observe with three dimensional model to what extent the climate of present earth is stable to the variation of the solar constant. The present concern is to assess the calculation possibility of the evaporation or the freezing of the oceans.

The second target includes so called aqua-planet experiment, where all of the lower boundary surface is assumed to be covered by the ocean[3-5]. The aim is to answer the basic problem of the climate, that is, "where and how does it rain?". In the aqua-planet experiments performed so far, the focus has been placed on especially in searching for the idealistic precipitation distribution of the tropics. The experiment performed here is also in this category, however, the new feature is to find out the deformation of the precipitation distribution to a warm SST (sea surface temperature) anomaly placed in the tropics. The configuration is supposed to extract the effect of the warm SST region in the real Western Pacific on the general circulation patterns.

The third target is to refine the dynamical framework of the rotating spherical convection theory, and also to acquire the description ability of the circulation patterns of the deep "atmospheres" as those of outer planets and the sun. The theory of convection in rotating spherical shells has been intensely considered by Busse and his colleagues[6]. The difficulty in their work is that the description utilized is too much mathematical, and hence it is not easy to acquire physical insight. Especially for the distribution of the angular momentum, there has not been presented any satisfactory mechanistic description.

Our activity recent years has been focused on the first target described above. We have performed the

parameter study of the aqua planet situation with varying solar flux and following conclusions are obtained:

1. the equilibrium state of three-dimensional atmosphere diminishes (the runaway greenhouse state is realized) when the solar constant S exceeds 1600 W/m^2 .
2. the meridional temperature difference decreases as the solar constant increases.
3. three-dimensional runaway limit is determined by the condition that one-dimensional equilibrium solution, in which relative humidity is taken into account, can exist.

In this year, we investigate the meridional energy transport in order to study in detail the change of the atmospheric structure with varying solar flux.

2. Experimental design

2.1 Model

The model utilized is basically the same as that used in [4]. It is the code originally produced by Dr. Numaguti of CCSR, and is the version now archived and maintained by GFD-DENNOU CLUB. The model consists of the three dimensional hydrostatic system on a sphere with very crude physical processes. The dynamical part is represented by the pseudo spectral method with the triangular truncation at wavenumber 21 (T21) and 32 vertical levels. The horizontal resolution might be crucially low but still is able to represent baroclinic instability.

The cumulus parameterizations are Kuo scheme or adjustment scheme or large scale condensation only. In this report, we will describe only the results with adjustment scheme. The vertical diffusion is represented by Yamada-Meller Level II scheme. The surface fluxes are evaluated by the usual bulk formula.

The surface is all covered by the ocean (aqua-planet). The value of SST is determined by the surface heat budget. The surface has no heat capacity; it is so called swamp ocean.

The radiation processes utilized is the exactly the same one as that of [2]. There is no scattering. Only the water vapor absorption of long wave radiation is included. Moreover, the absorption coefficient is constant (gray atmosphere). The sun is assumed to be at the equinox position. Hence the zonal mean incoming solar flux is symmetric around the equator.

In order to enable the longer term integration of the runaway greenhouse state, we have to introduce Rayleigh damping and Newtonian cooling in the upper 7 layers, and moreover we have to introduce a vertical smoothing filter similar to [8] in temperature and horizontal wind fields.

2.2 Experimental Design

The investigation performed this year is the analyses of the results of parameter study with various solar flux. The values of the solar flux S are, 1200 W/m^2 , 1380 W/m^2 , 1500 W/m^2 , 1550 W/m^2 , 1570 W/m^2 , 1600 W/m^2 , 1700 W/m^2 , 1800 W/m^2 . The initial condition for each experiment is the rest atmosphere with the homogeneous temperature (280K) and homogeneous specific humidity (10^{-5}). The data from day 950 to 1000 are utilized for analyses.

In 3.1, we will briefly show the results of our calculation and discuss the meridional temperature difference and its relation to the value of runaway limit. We will show the the dependency of the meridional energy transport on the solar flux in 3.2 and discuss the mechanism of energy transport in 3.3.

3. The Results of the experiments for varying solar flux

3.1 The runaway limit of three-dimensional grey atmosphere

The most important result of our parameter study is sammarized in Figure 1, where the relationship between the global mean OLR(Outgoing Longwave Radiation) and global mean inward solar flux is shown. When the value of the global mean inward flux is less than 392.5 W/m^2 (S = 1570 W/m^2), the global mean value of OLR almost equal to that of inward flux and the system reaches equilibrium states. However, in cases with the global mean solar flux larger than 400 W/m^2 (S = 1600 W/m^2), that of OLR becomes less than 350 W/m^2 . In those cases, both of the ground temperature and moisture content increase and the runaway greenhouse states occur. Figure 1 suggests that the value of runaway limit of the three-dimensional gray atmosphere is about S = 1600 W/m^2 .

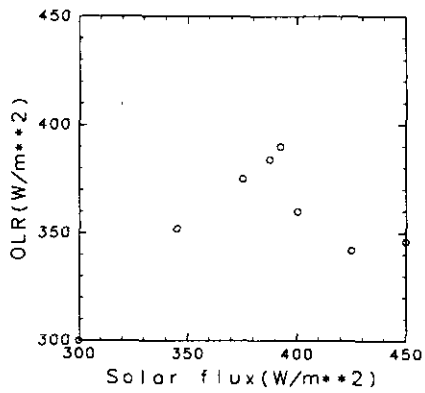

Figure 1. The relationship between the global mean inward solar flux and the calculated global mean OLR.

Figure 2 shows the zonally averaged OLR for the equilibrium states of the cases where S = 1200 W/m^2, S = 1380 W/m^2, S = 1500 W/m^2, S = 1550 W/m^2 and S = 1570W/m^2. Figure 2 indicates that the value of tropical OLR is quenched to 400 W/m^2 when the global mean solar flux exceeds 375 W/m^2. The values of OLR in the higher latitudes also approach 400 W/m^2 as the solar flux increases. The latitudinal difference of the ground temperature also decreases (Figure 3). These tendencies indicate that the realization of the runaway greenhouse state depends on whether the global mean

value of inward solar flux exceeds the the asymptotic value of OLR, 400 W/m^2 .

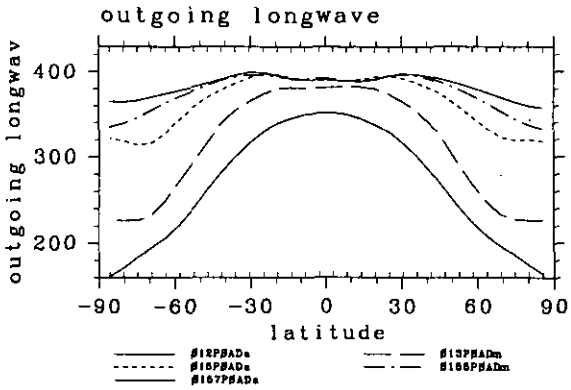

Figure 2. The latitudinal distribution of OLR for various solar flux. The values of the solar flux are 1570 W/m^2, 1550 W/m^2, 1500 W/m^2, 1380 W/m^2, 1200 W/m^2.

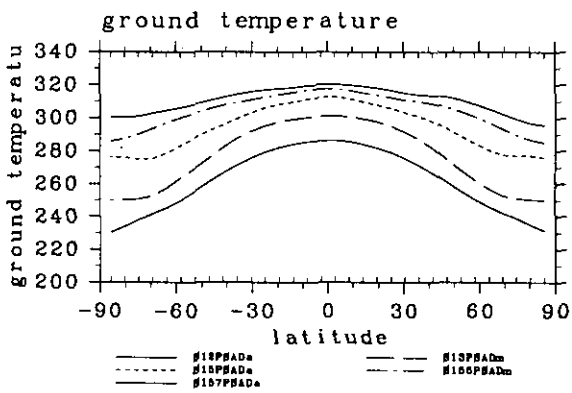

Figure 3. Same as Figure 4 except for the ground temperature.

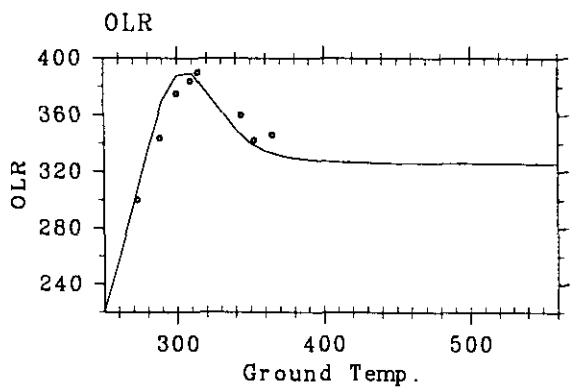

Figure 4. The relationship between the surface temperature and OLR. The solid line represents the solution of the one-dimensional radiative-convective equilibrium model with the relative humidity 60 %. The circles are the global mean values obtained by GCM.

In order to consider the asymptotic value of OLR, we compare the results of three-dimensional calculations with those of one-dimensional model. Figure 4 shows the relationship between the surface temperature and OLR of the one-dimensional radiative-convective equilibrium solutions with the relative humidity 60 %. In this figure, the global mean values obtained by the calculations with GCM are also plotted. The good agreement of three-dimensional results with the one-dimensional solutions suggests that the asymptotic value of OLR shown in Figure 2, which is the runaway limit of the three-dimensional atmosphere, equals to the radiation limit of the one-dimensional solution in which the value of the relative humidity is taken into account.

3.2 The energy transport in the equilibrium states

The result that the meridional temperature difference decreases with increasing solar flux suggests that the energy transport shouod increase with the solar flux. In this section, we investigate the change of the magnitude of energy transport for varying solar flux and clarify the substances that contribute to that change. Figures 5 ~ 8 show the northward transports of dry static energy and latent heat in cases of S = 1380 W/m^2 and S = 1570 W/m^2 . Each figure shows the total transport

$$\int_0^1 [\overline{X \cdot v}]d\sigma, \tag{1}$$

the contribution of the mean meridional circulation

$$\int_0^1 [\overline{X}][\overline{v}]d\sigma, \tag{2}$$

the contribution of the stationary eddies

$$\int_0^1 [\overline{X^* v^*}]d\sigma, \tag{3}$$

the contribution of the transient eddies

$$\int_0^1 [\overline{X' \cdot v'}]d\sigma, \tag{4}$$

where X is either dry static energy or latent heat, v is northward velocity, $^-$ denotes the time mean value, [ ] denotes the zonal mean value, * denotes the deviation from its zonal mean, $'$ denotes the deviation from its time mean.

In case of S = 1380 W/m^2 , the magnitudes of the dry static energy transport and the latent heat transport are almost the same (Figures 5 and 6). The dry static energy is transported mainly by the mean meridional circulation and the transient eddies. As for the latent heat, the transport by the transient eddies is dominant. The actual structure of the transient eddies is considered to be baroclinic instability. However, in case of S = 1570 W/m^2 , the magnitude of the latent heat transport exceeds that of the dry static energy transport (Figures 7 and 8). The dominant contributors to the latent heat transport is the transient eddies, which is the same as the case with S = 1380 W/m^2 . This result suggests that the increase of the poleward

energy transport is accounted for by the intensification of the activity of transient eddies.

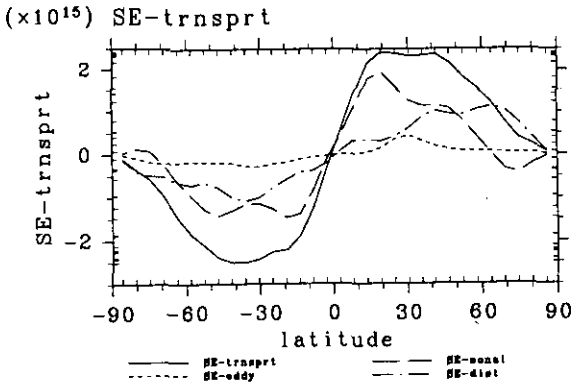

Figure 5. The northward transport of the dry static energy in case with $S = 1380$ W/m^2 . The solid, dashed, dotted and dash-dotted lines are total transport, the contribution of the mean meridional circulation, the contribution of the stationary eddies, the contribution of the transient eddies, respectively.

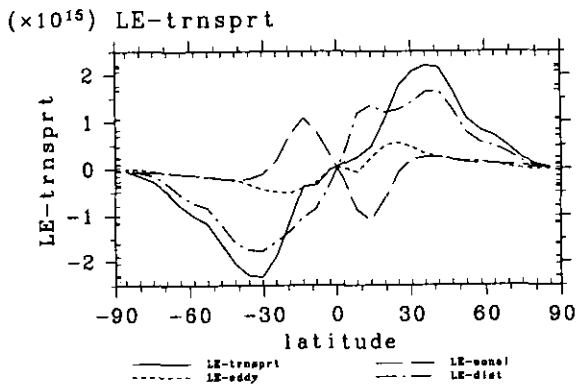

Figure 6. Same as Figure 5 except for the northward transport of the latent heat.

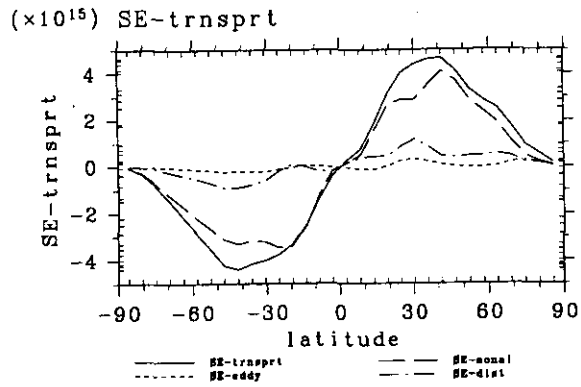

Figure 7. Same as Figure 5 except for $S = 1570$ W/m^2 .

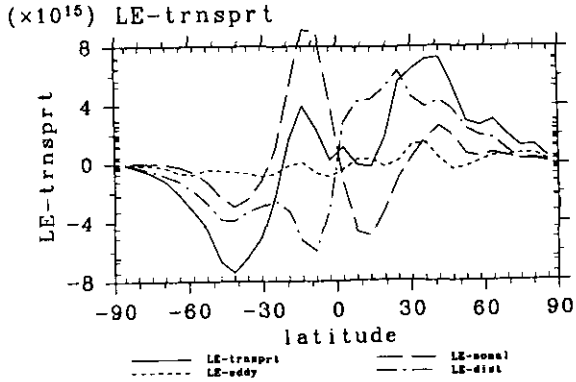

Figure 8. Same as Figure 7 except for the northward transport of the latent heat.

3.3 The features of the transient eddies

Figures 9 and 10 show the horizontal distributions of precipitation in cases of $S = 1380$ W/m^2 and $S = 1570$ W/m^2 , respectively. Both figures show the snap shots of several days after the equilibrium states are established.

In case of $S = 1380$ W/m^2 , there exist two kind of major features; the eastward propagating disturbances which are considered to be baroclinic instability and the vortex structures which are considered to be tropical cyclones. The vortex structures sometimes move from equatorial region to mid-latitudes. An example of the vortex structure is found at $(20°, 20°)$ in 1059 day (the top figure of Figure 9). This disturbance moves to $(40°, 30°)$ in 1063 day and to $(110°, 70°)$ in 1063 day.

In case of 1570 W/m^2 , the dominant precipitation activity in the mid-latitudes is the vortex structure moving from the equatorial region. The most of precipitation at 40 degree latitudes is associated with those vortex structures. An example of the precipitation area is located at $(220°, 15°)$ in 1008 day, which moves to $(260°, 25°)$ in 1012 day and to $(315°, 40°)$ in 1016 day. The increase of poleward energy transport with the increase of the solar flux discussed in 3.2 is accounted for by latent heat transport of the intense activity of the tropical cyclones.

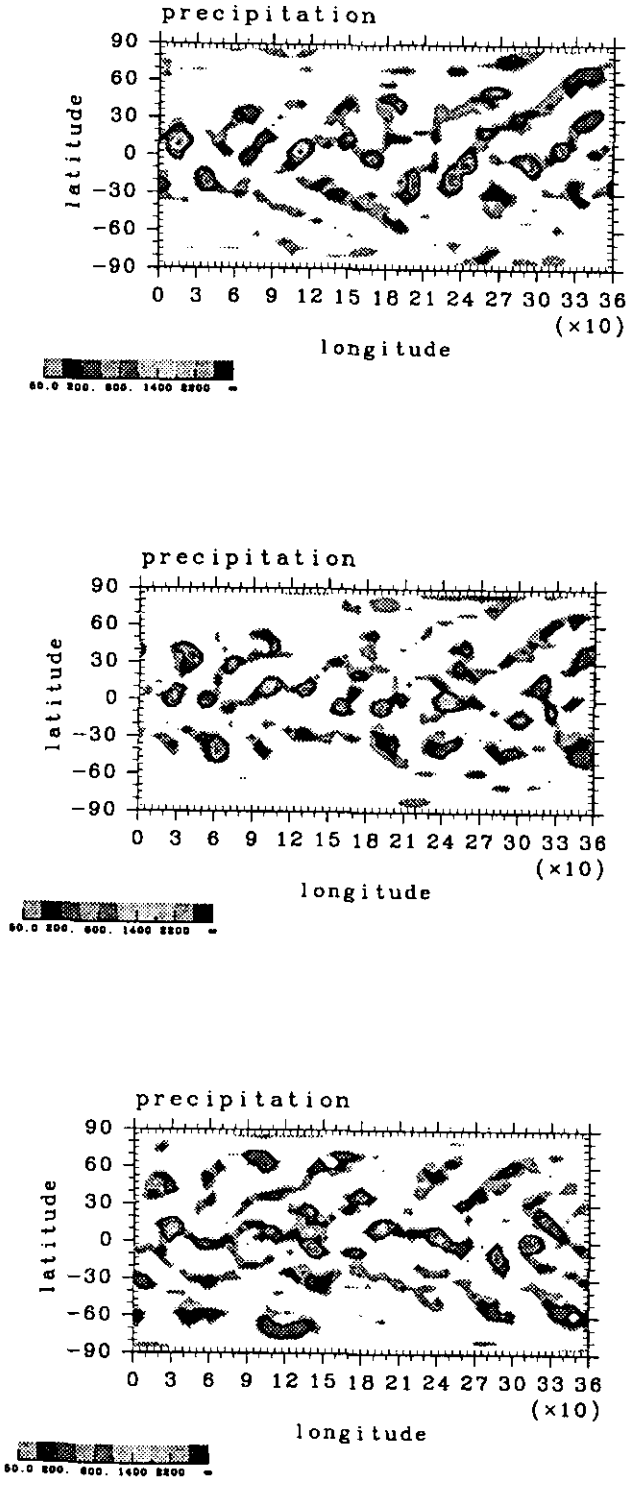

Figure 9. The snap shots of horizontal distribution of precipitation in the case with $S = 1380$ W/m^2 . The top, middle, and bottom figures show the distributions at 1059 day, 1063 day, 1067 day, respectively.

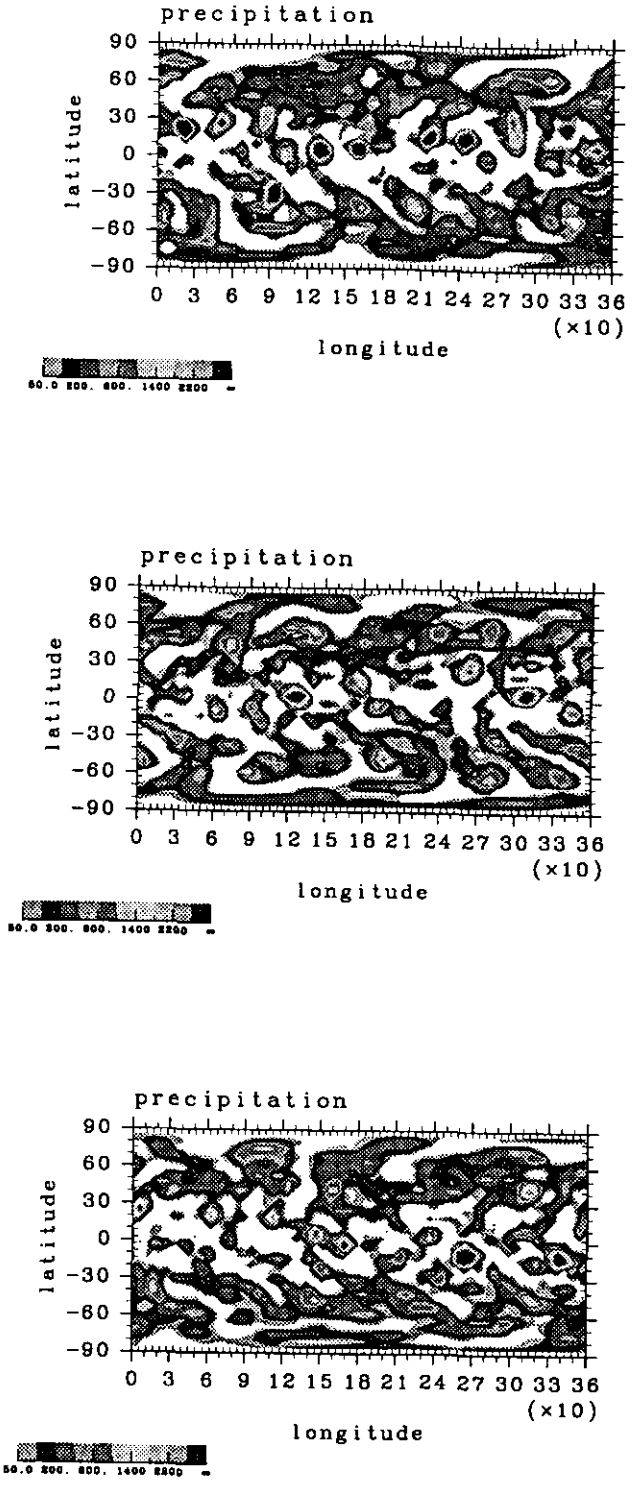

Figure 10. The snap shots of horizontal distribution precipitation in the case with $S = 1570$ W/m^2 . The top, middle, and bottom figures show the distributions at 1008 day, 1012 day, 1016 day, respectively.

Acknowledgment

We wish to thank Drs. Fukuwatari, Nakata, and ohter staff members of CGER for providing us with this powerful computing facility. Our software environment was provided from the resources of GFD DENNOU CLUB. GFD DENNOU CLUB is an independent group of scientists aiming at collecting basic software resources for research and education of geophysical fluid dynamics and related fields. Those resources include three dimensional spherical primitive system originally developed by Dr. Numaguti while he was at University of Tokyo.

References

1. G.S. Golitsyn, *ICARUS*, **13**, 1 (1970)
2. S. Nakajima, Y.-Y. Hayashi and Y. Abe, *J. Atmos. Sci.*, **49**, 2256 (1992)
3. Y.-Y. Hayashi and A. Sumi, *J. Met. Soc. Japan*, **64**, 451 (1986)
4. A. Numaguti and Y.-Y. Hayashi, *J. Met. Soc. Japan*, **69**, 541 (1991)
5. A. Numaguti, *J. Atmos. Sci.*, **50**, 1874 (1993)
6. K.-K. Zhang and F.H. Busse, *Geophys. Astrophys. Fluid Dynamics.*, **39**, 119 (1987)
7. E. Manzini and K. Hamilton, *J. Atmos. Sci.*, **50**, 2180 (1993)
8. R. Shaprio, 1971: *J. Atmos. Sci.*, **28**, 523.

Direct Numerical Simulation of Drag Forces on Wavy Walls

Contact Person Professor, Satoru Komori
Dept. of Chemical Engineering, Kyushu University

(Research Organization) PhD Student, Takashi Shimada
Dept. of Chemical Engineering, Kyushu University

Research Associate, Kouji Nagata
Dept. of Chemical Engineering, Kyushu University

Section Head, Shunji Takeshita
National Institute for Environmental Studies,
Environmental Agency of Japan

Senior Scientist, Kunio Kohata
National Institute for Environmental Studies,
Environmental Agency of Japan

Keywords friction drag, pressure drag, wavy wall, DNS, turbulence structure, air-water interface

1. Introduction

It is of great importance to propose a model to precisely estimate heat and mass exchange velocities across the wind-induced wavy air-sea interface in relation to the reliable predictions of global warming and unusual climate (Komori *et al.*,1993a). Moreover, models for accurately estimating heat and mass transfer rates across the wavy gas-liquid interface are desired to develop industrial equipment such as evaporation, condensation and gas absorption equipment. In the previous studies, heat and mass transfer velocities have been estimated using the relations with the wind friction velocity on the gas side. The friction velocity was experimentally obtained from the measurement of a peak value of the Reynolds stress in the vicinity of the air-water interface or by using the log-low of the mean velocity in the fully-developed turbulent region over the interface. However, it is not certain whether the empirical friction velocity really represents the fluid shear acting on the interface. Because for the wavy air-water interface the contribution of the form drag to the total drag increases compared to that of the friction drag. If the empirical friction velocity involves the large contribution of the form drag, the relations between the heat and mass transfer velocities and the friction velocity are not useful for estimating the transfer velocities under arbitrary interfacial conditions.

The purpose of this study is, therefore, to investigate whether the conventional experimental methods for estimating the friction velocity for the wavy air-water interface really represents the friction drag on the interface by using a three-dimensional direct numerical simulation (DNS). The air flow over the air-water interface was regarded as being similar to the turbulent flow over wavy walls, since the wind speed is very faster than the wave velocity. For the actual gas-liquid interface two-dimensional and three-dimensional waves are observed in the low and high wind speed reigins, respectively. The DNS was, therefore, applied to flows over both two- and three-dimensional wavy walls. The friction and form drags predicted by the DNS were compared with the values estimated from the DNS's data by using the conventional experimental methods based on the Reynolds stress and the log-law.

2. Numerical Simulation

The three-dimensional Navier-Stokes (N-S) equations were directly solved using a marker and cell method in the computational domain (Fig.1). The nonlinear terms appeared in the N-S equation were discretized by a fifth-order upwind scheme and other spatial derivatives were discretized by a sec-

ond-order central difference (Komori *et al.*,1993b). The wave amplitude and length corresponded to the actual wind-wave which was observed for the wind speed of 5m/s in a wind-wave tank. The ratio of the wave height to the wave length λ was 0.07. The streamwise (x), spanwise (y) and vertical (z) sizes of the computatinal domain were 4δ, 4δ and δ, respectively. The grid points were $101 \times 101 \times 60$ in x, y and z directions, and the boundary-fit coordinate system was used (Komori *et al.* 1993b). The Reynolds number Re based on the uniform velocity U and the characteristic length δ was about 4,000.

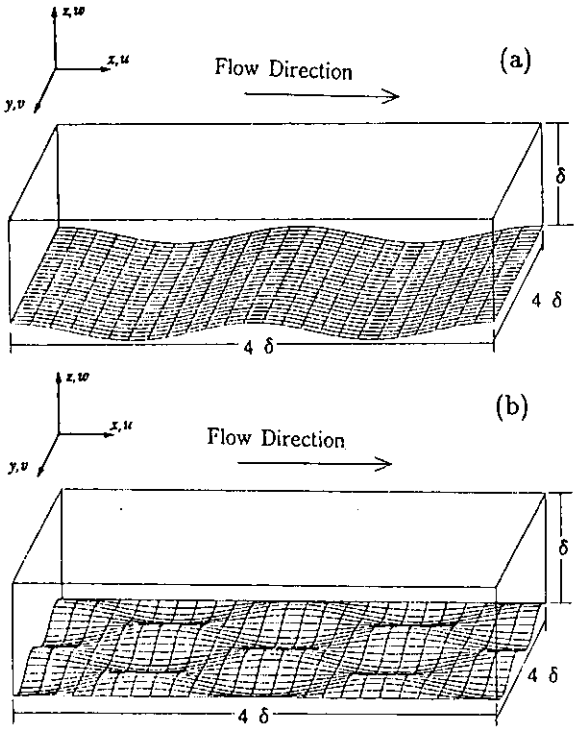

Figure 1. Schematic of the computational domain. (a) Two-dimensional wavy wall ; (b) Three-dimensional wavy wall

3. Results and Discussion

3.1 Drag acting on the wavy walls

Pressure drag D_p and friction drag D_f which act on two- and three-dimensional wavy wall are defined by

$$D_p = \int_{A_p} p\, dA_p \tag{1}$$

$$D_f = \int_{A_f} \mu \frac{du}{dz}\, dA_f \tag{2}$$

where A_p and A_f show the projected areas to the streamwise direction (x) and to the perpendicular direction of (z) of the wavy wall, respectively. The pressure and friction drags calculated by Eqs.(1) and (2) are listed in Table 1. The ratio of the pressure drag to the total drag is 0.54 for the two-dimensional wavy wall, and the pressure drag is larger than the friction drag. On the other hand, the ratio of the friction drag to the total drag is 0.75 for the three-dimensional wavy wall and the friction drag exceeds the pressure drag. The ratios of the friction drag to the pressure drag are 2.9 and 0.86 for two- and three-dimensional wavy walls, respectively.

	Two-dim. wavy wall	Three-dim. wavy wall
Pressure drag [N]	1.59×10^{-4}	5.99×10^{-5}
Friction drag [N]	1.37×10^{-4}	1.76×10^{-4}
Total drag [N]	2.96×10^{-4}	2.36×10^{-4}
Friction drag /Total drag [-]	0.46	0.75

Table 1. Pressure and friction drags acting on wavy walls

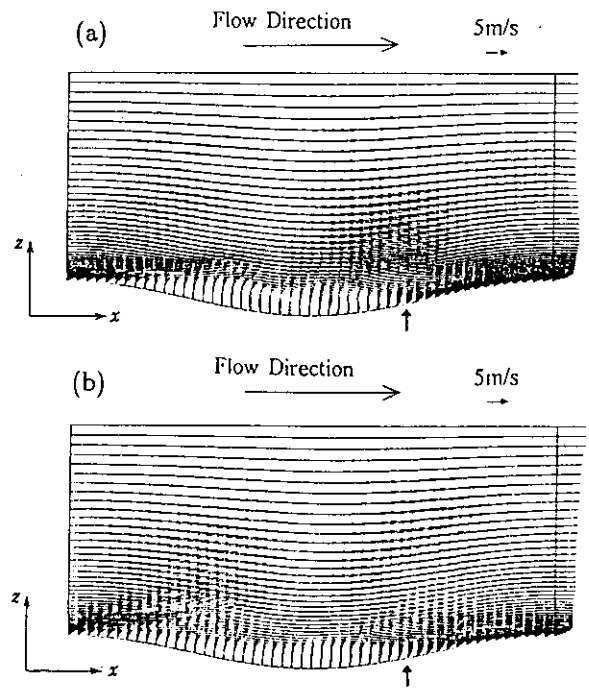

Figure 2. Instantaneous velocity vectors on the x-z plane. (a) Two-dimensional wavy wall. ; (b) Three-dimensional wavy wall.

In the field of oceanography, it has been controversial which drag is dominant for the wind-induced wavy air-water interface (e.g. Banner and Peirson (1995)). The values in Table 1 suggest that the ratio of the pressure drag or the friction drag to the total drag strongly depends on whether the wave shape is two-dimensional or

three-dimensional. In other words the pressure drag is comparable to the friction drag for two-dimensional wind-waves in the low wind speed region, and the ratio of the friction drag to the total drag increases with the three-dimensionality in the high wind speed region. Figure 2 shows the vectors of instantaneous velocity over the wavy walls. The velocity vectors over the two-dimensional wavy wall show that a circulating flow due to flow separation appears beyond the wave crest. They also suggest that the high pressure acts on the wall where the flow reattaches. On the other hand, the flow over the three-dimensional wavy wall passes around the crests and therefore the circulating flow is very weak. The flow structures explain why the ratio of the friction drag to the form drag drastically changes between two- and three-dimensional wavy walls.

3.2 Friction velocity

Figures 3 and 4 show the distributions of the time-averaged velocity and the Reynolds stress over the two- and three-dimensional wavy walls, together with the values over a flat plate. The friction velocity was estimated from these distributions by using the same two methods as used in experimental studies. The first method estimated the friction velocity from the gradient of the logarithmic velocity distribution in the region of $z > 0.006$m ($z^+ > 100$) (see straight lines in Fig.3). The second method estimated the friction velocity from a peak value of the Reynolds stress over the wall (Komori *et al.* 1993a ; Kawamura and Toba, 1988). The friction velocities estimated by these methods are listed in Table 2, together with the real friction velocity directly calculated from the gradient of the instantaneous velocity on the wall by Eq.(2).

Friction velocities estimated by the log-law and Reynolds stress methods are about 9 % and 4% larger than the real friction velocity for the two- and three-dimensional wavy walls, respectively. Of course, the friction velocity estimated by the log-law for a flat plate has the same value as the real friction velocity, since the pressure drag is absent. The results suggest that the conventional empirical methods for estimating the friction velocity are rather applicable to wavy air-water interfaces, but they considerably overestimate the friction velocity for two-dimensional waves with larger wave height.

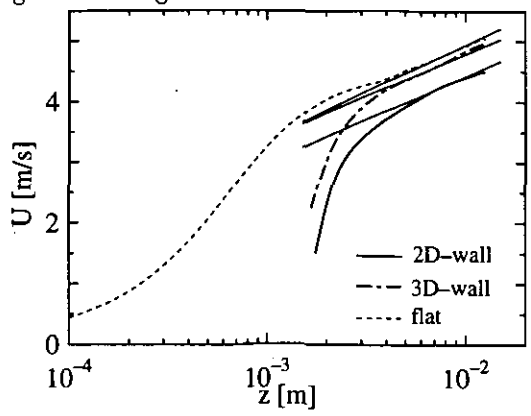

Figure 3. Distributions of mean velocity on wavy walls.

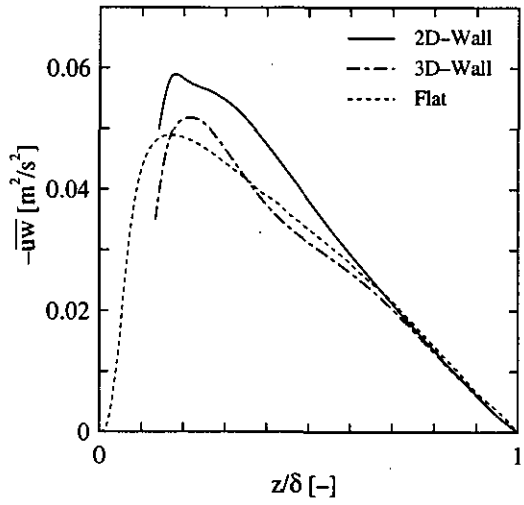

Figure 4. Distributions of the Reynolds stress on wavy walls.

	Log-law method u^* [m/s]	Reynolds stress method u^* [m/s]	By Eq.(2) u^* [m/s]
Two-dim.	0.25	0.25	0.23
Three-dim.	0.24	0.23	0.23
Flat plate	0.27	0.22	0.27

Table 2. Comparison of the friction velocity calculated by Eq.(2) with that estimated by conventional methods

Acknowledgements

The computation was carried out by the super computer SX-3 of Central for Grobal Environmental Research, National Institute for Environmental Studies.

References

1. Banner, M.L. and Peirson,W.L. : An Observational Study of the Aqueous Surface Layer Structure beneath a Wind-Driven Air-Water Interface, *Air-Water Gas Transfer*, B.Jahne and E.C.Monahan,eds., AEON Verlag & Studio,Hanau, (1995), 115-124.
2. Kawamura, H. and Toba, Y. : Ordered Motion in the Turbulent Boundary Layer over Wind Waves, *J. Fluid Mech.* **197** (1988), 105-138.
3. Komori, S. : Turbulence Structure and CO_2 Transfer at the Air-Sea Interface and Turbulent Diffusion in Thermally-Stratified Flows, CGER'S Supercomputer monograph Report, vol.1, Center for Global Environmental Research, National Institute for Environmental Studies, Environment Agency of Japan (1996).
4. Komori, S., Nagaosa, R. and Murakami, Y. : Turbulence Structure and Mass Transfer across a Sheared Air-Water Interface in a Wind-Driven Turbulence, *J. Fluid Mech.* **249** (1993a), 161-183.
5. Komori, S., Nagaosa, R., Murakami,Y., Chiba,M., Ishii, K. and Kuwahara, K. : Direct Numerical Simulation of Three-Dimentional Open-Channel Flow with Zero-Shear Gas-Liquid Interface, *Phys. Fluids A* **5** (1993b), 115-125.
6. Okuda, K., Kawai, S. and Toba, Y : Measurement of Skin Friction Distribution along the Surface of Wind Waves, *J. Oceanogr. Soc. Jap.* **30** (1977), 190-198.

Three-dimensional polar vortex structure in a stratified rotating fluid

Contact Person Takesi Miyazaki
1-5-1 choufugaoka choufushi tokyo
Research Organization Hirofumi Shinkawa
Masahiro Shimada

Keyword polar vortex , filamentation , quasi-geostrophic model , N-layer model

1 Introduction

The robustness of the stratospheric polar vortex is an issue of great concern because it bears strongly on ozone depletion. It is, however, well known that thin stream of vorticity is ejected repeatedly from the polar vortex and that it breakes down in early spring. The low ozone parcel might be transported to midlatitude area. The two-dimensional vortex filamentation and collapse have been investigated numerically by McWilliams[1] (spectral method) and Dritschel [2](contour surgery). Since the polar vortex has a three-dimensional structure , we incorpolate the three-dimensionality by extending the two-dimensional spectral code developed at KUDPC to quasi-geostrophic- and N-layer-codes. Polvani[3] performed a two-layer simulation and showed that two vortices in different layers aligned. We compare our computational results on a spherical surface with theirs.

2 Numerical method

2.1 Vorticity equation

The quasi-geostrophic fluid motions in a rotating stably stratified fluid are described by the following vorticity equation

$$\frac{\partial}{\partial t}q = -\frac{\partial\psi}{\cos\phi\,\partial\theta}\frac{\partial q}{\partial\phi} + \frac{\partial q}{\cos\phi\,\partial\theta}\frac{\partial\psi}{\partial\phi} -2\frac{\partial\psi}{\partial\theta} + \nu\nabla^2 q \qquad (1)$$

ϕ : longitude ν : kinematic viscosity
θ : latitude ψ : stream function
t : time q :potential vorticity

where the potential vorticity:q is expressed as ,

$$q = \nabla^2\psi + F \qquad (2)$$

Here F denotes the baroclinic term of potential vorticity. We consider the following two models. The first is the quasi-geostrophic model (Q-G), in which the density is continuously stratified . In the Q-G model , F is expressed following.

$$F = \frac{1}{\rho}\frac{\partial}{\partial z}\left\{\frac{\rho}{S}\left(\frac{\partial\psi}{\partial z}\right)\right\} \qquad (3)$$

ρ is the fluid density , S is a stratification-parameter.

$$S = \frac{N_0^2 D^2}{f_0^2 L^2} \qquad (4)$$

f_0 :Coriolis parameter
L :horizontal length-scale
D :vertical length-scale
N_0 :*Brunt-Väisälä* frequency

The second , which is a simplification of Q-G ,is the N-layer model. The fluid is composed of N layers , each of which consists of fluid of uniform , constant density ρ_n. In the N-layer model , F is expressed following.

$$F = -\frac{DF_n}{\frac{\Delta\rho}{\rho_0}}\left(\frac{2\psi_n - \psi_{n+1} - \psi_{n-1}}{D_n}\right) \qquad (5)$$

F_n is expressed following .

$$F_n \equiv \frac{f_0^2 L^2}{gD}. \qquad (6)$$

D_n : height of the nth layer
ρ_0 :characteristic fluid density
$\Delta\rho$:density difference between adjacent layers

2.2 Spectral transformation and truncation

We use the Fourier-Legendre expansions in the horizonal discretization and the central difference in the vertical discretization. The number of grid points in the longitude direction is NLON=256 and that in the latitude direction is NLAT=128 . The truncation wave number is MT=85 (T85) . In the Q-G model , the number of vertical grid points is 39 , whereas we consider a 2-layer model in the following N-layer calculations .

2.3 Time marching

We have tried the Adams-Bashforth and the Runge-Kutta method in the time-marching .No significant difference has been observed between the results obtained using these two schemes. So , we use the former scheme in order to shorten the computation time .

3 Results

3.1 Quasi-geostrophic model

The time-development of an elliptical vortex , which is sligtly displaced from the pole , is shown in Fig.1. Here , the time-evolution in the midlayer (K=20) is depicted . Continual emission of thin filaments is observed. Figure 2 shows the vertical structure of filamentation in a meridian cross section. The emission is fastest in the midlayer , since we have assumed that the vertical vorticity profile is propotional to $\sin^2\frac{K}{K_{max}}\pi$ which is consistent with the upper and lower boundary conditions : $\frac{\partial\psi}{\partial z} = 0$.

3.2 N-layer model

We tried to reproduce the alignment observed in the two-layer (plane) computation by Polvani . In fact , two vortex patches in the upper and lower layers align near the pole (Fig.3). It is , however , shown that a single vortex patch moves to the pole due to the β effect. We performed numerical simulations without the Coliolis term in order to assess the effect of interactions between the vortices (Fig.4). In this case the alignment occurs , too , but much more slowly. The β effect gives a larger influence to the vortex dynamics near the pole.

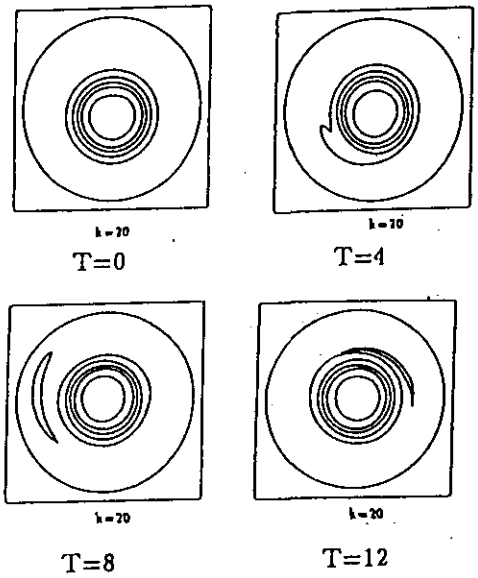

Figure 1: time-development of deformed vortex

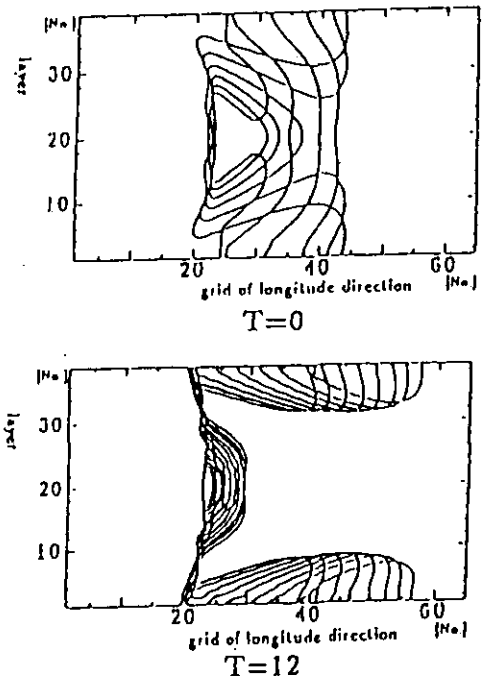

Figure 2: vorticity profile in vertical direction

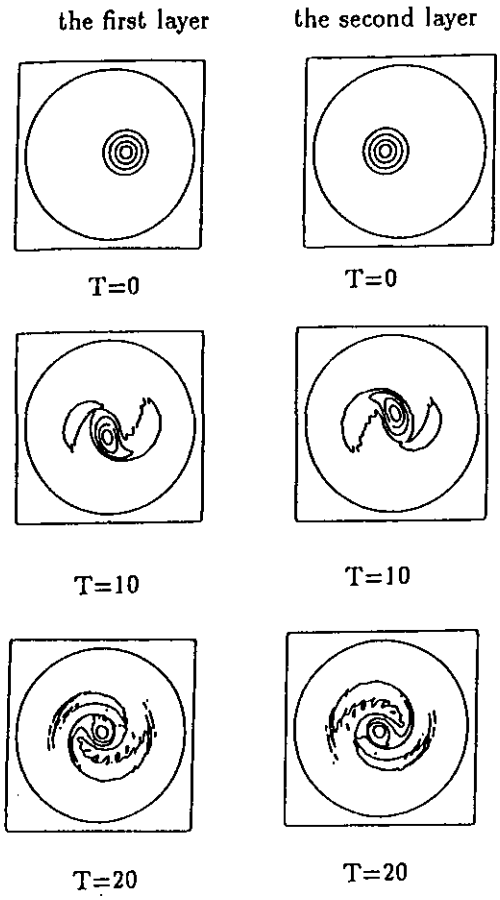

Figure 3: alignment

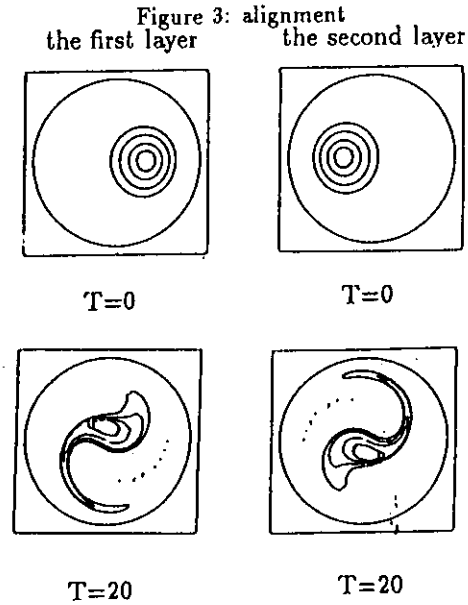

Figure 4: alignment

4 References

1. J.C. McWilliams,1990 *J.Fluid Mech.* vol.219, 361-385
2. D.G. Dritschel,1995 *J.Fluid Mech.* vol.293, 269-303
3. L.M. Polvani, 1991 *J.Fluid Mech.* vol.225, 241-270

Direct Numerical Simulation on Spiral Taylor-Görtler Vortex in Spherical Couette Flow

Contact Person *Weiming Sha*
Department of Mechanical Engineering
Nagoya Institute of Technology, Japan
Research Organization *Hiromasa Ueda*
Disaster Prevention Research Institute
Kyoto University, Japan
Keywords Direct Numerical Simulation, Spiral Taylor-Görtler vortex
Spherical Couette Flow

1. *Introduction*

In this paper, we use a finite-difference scheme[1] to solve the three dimensional incompressible time-dependent Navier-Stokes equations in spherical polar coordinate. Singularities of the Navier-Stokes equations in spherical polar coordinates can be removed by performing spatial discretization on a conservative form of the equations on a staggered grid. Based on Dukowicz and Dvinsky's approximate factorization method[2], a new algorithm, which is a second-order accurate in time and space, are given. The Taylor-Görtler vortex of the spherical Couette flow is then simulated with this numerical method. So far as we know, there is still no literature on the work. In the following, the governing equations and boundary conditions are presented in Section 2. The numerical method is described briefly in Section 3. In Section 4, we show some numerical results of the Taylor-Görtler vortex in the spherical Couette flow of the spherical Couette flow, and a comparison with experimental measurements. A summary is given in Section 5.

2. *Governing Equations and Boundary Conditions*

The full incompressible Navier-Stokes equations with no body force and the continuity equation are

$$\frac{\partial \mathbf{u}}{\partial t} + \mathbf{u} \cdot \nabla \mathbf{u} = -\nabla p + \frac{1}{Re} \nabla^2 \mathbf{u} \qquad (2.1)$$

$$\nabla \cdot \mathbf{u} = 0 \qquad (2.2)$$

where $\mathbf{u}$ is the velocity field, p is kinematic pressure and Re is the Reynolds number.

We consider the time-dependent motion of an isothermal, incompressible, Newtonian fluid contained in an annulus between two concentric rotating spheres. The spheres are assumed to be rigid and the cavity region between the spheres is fulled with a viscous fluid. The inner sphere is constrained to rotate about the vertical axis with a prescribed angular velocity Ω, while the outer sphere is fixed. The inner and outer radii of the spheres are R_1 and R_2, respectively. The Reynolds number is defined as $Re = \frac{\Omega R_1^2}{\nu}$ which ν is the kinematic viscosity.

No-slip (rigid) boundary conditions along the spherical boundaries are

$$u_r = u_\theta = 0,\ u_\varphi = \sin\theta \quad \text{on } r = R_1,$$

$$u_r = u_\theta = u_\varphi = 0 \quad \text{on } r = R_2.$$

3. *Numerical Method*

The numerical method is the same as that in [1]. The numerical method is only described briefly here.

Space discretization is carried out in a computational domain between the two concentric spheres, and the unknown discrete variables are referred to the nodes in the interior, not to the boundary nodes. The spatial discrete operators are evaluated using the central finite-difference scheme on a staggered grid, and are second-order accurate in space. For the time-integration, we have used a semi-implicit time-advancement scheme with the implicit Crank-Nicolson scheme for the conservative part of the viscous term and the explicit Adams-Bashforth scheme for the convective and the remained viscous terms. The pressure term is treated in a mixed form of the Crank-Nicolson and Adams-Bashforth scheme. The discretization of the method is second-order

accurate in time and space.

The approximate factorization technique (Beam and Warming [3]; Briley and McDonald [4]; Kim and Moin [5] is used to treat the discrete velocity equation and, we compute the discrete velocity of equation by solving three tridiagonal matrices with a standard TDMA(TriDiagonal-Matrix Algorithm) method. As for the discrete pressure, we can compute it firstly by application of ADI (Alternating-Direction Implicit) method (Peaceman and Rachford [6]) to the discrete pressure equation, and then solving the system with a standard TDMA method for the two tridiagonal matrices and with a refined TDMA method(Temperton [7]) for the cyclic tridiagonal matrix.

To complete the numerical method, adequate initial conditions of the velocity $\mathbf{u}^0$ and the pressure gradient Gp^0 are required. In the present study, we chose the Stokes solution as the initial velocity condition at Re=5, i.e., $\mathbf{u}^0=\mathbf{u}^0(0, 0, u_\phi{}^0)$ in which the Stokes flow profile is

$$u_\phi{}^0=\frac{1}{(1+\beta)^3-1}\left(-r+\frac{(1+\beta)^3}{r^2}\right)\sin\theta$$

where the clearance ratio ß is defined as $ß=(R_2-R_1)/R_1$. This Stokes flow is the time-independent, axisymmetric solution to the equations (2.1)~(2..2) and the boundary condition in the limit Re ---> 0. For the initial pressure gradient it can be found that $Gp^0=0$ is exactly satisfied in this Stokes solution of the spherical Couette flow. When considering a steady, low Reynolds number flow as the initial state, we generally have the relation $GP^0=\nabla^2\mathbf{u}^0/Re$ for the initial pressure condition.

In the following calculation, the computational domain is divided by a number of grids 22*361*91 in the radial, meridional and circumferential directions, respectively. The grids were constructed uniformly in the meridional and circumferential directions, while a geometric distribution was used in the radial direction in order to improve the resolution in the near-wall region of the spheres.

Since the viscous stability limit is removed by treating the conservative part of the viscous terms implicitly, the stability of the overall numerical method is restricted by the CFL condition. The local CFL number is defined as

$$CFL=\left(\frac{|u_r|}{\Delta r}+\frac{|u_\theta|}{r\Delta\theta}+\frac{|u_\phi|}{r\sin\theta\,\Delta\phi}\right)\Delta t$$

where Δr, $r\Delta\theta$ and $r\sin\theta\Delta\phi$ are the grid spacing of the spherical polar coordinates. The time increment Δt is then required for the restricted stability condition of max{CFL}<1 where max{CFL} is the maximum value of CFL number evaluated in the computational domain. However, the condition of max{CFL}<1 here is only a guess but not a known stability limit.

In the next Section, we present the direct numerical simulation results in the case of ß=0.14. For comparison ß has been chosen as same as that in the experiments(Nakabayashi [8] , Nakabayashi and Tsuchida [9]). The Reynolds number was quasi-statically increased($dR^*/dt=0.0006$, R^* is defined as $R^*=Re/Rec$ in which Rec is the critical Reynolds number for occurrence of the Taylor-Görtler(TG) vortex) in order to eliminate the effect of the rotative acceleration ratio on the spherical Couette flow (Nakabayashi and Tsuchida [10]). Time integration was carried out until the steady or time-periodic state was obtained.

4. Numerical Results

In this section, we present the results on the numerical simulation of the so-called spiral Taylor-Görtler(TG) vortex (Nakabayashi [8]). Dumas and Leonaed[11] have been successful in simulation of the three-dimensional spiral TG vortices for a narrow gap case(ß=0.06). In this numerical simulation, we are concerned with ß=0.14 , a moderate gap case.

As we raise the Reynolds number Re to a higher value, the 1-vortex flow(TG vortex flow) becomes unstable due to the secondary instability, and its symmetry is broken. This secondary instability results in a transition from the 1-vortex flow to the supercritical spiral TG vortex flow. This three-dimensional spiral TG vortex flow at Re=Res=1110 (Res; the Reynolds number for occurrence of the spiral TG vortex) is illustrated in the following Fig. 1 and Fig. 2. First, Fig. 1 shows the plots of the velocity vectors(u_ϕ, u_θ) of the spiral TG vortex flow in the (θ, ϕ) spherical cross-section at mid-gap radius viewed from (a) $\phi=\pi/2-2\pi/9$; (b) $\phi=\pi-\pi/9$; (c) $\phi=3\pi/2-2\pi/9$; (d) $\phi=2\pi-2\pi/9$. The flow on the section moves in the same direction as that of the inner rotating sphere (counterclockwise). The contour of the zero radial velocity ($u_r=0$) in this section is also drawn with two types of solid lines, which is the boundary between existing inflow($u_r<0$) and outflow($u_r>0$). Thin solid lines indicate the center positions of the two toroidal TG vortices. The thick ones, which are counted by every two thick lines from each side of the equator, correspond to the center lines of the spiral TG vortices. Fig. 2 gives the bird's-eye view of the radial velocity(u_r) in the same

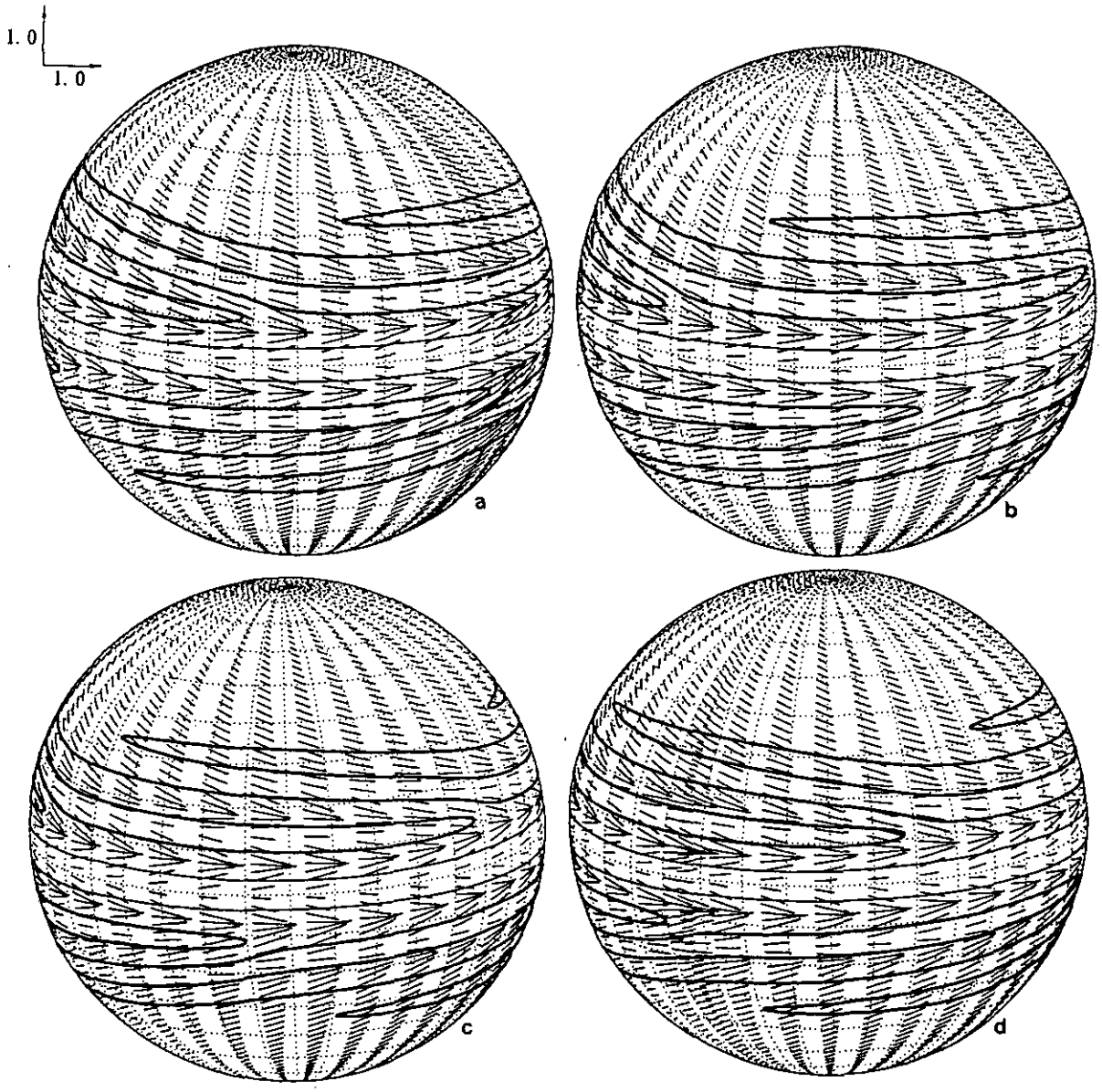

Fig. 1 Plots of the velocity vectors of the spiral TG vortex flow in the (θ, ϕ) spherical cross-section at mid-gap radius viewed from (a) $\phi=\pi/2-2\pi/9$; (b) $\phi=\pi-2\pi/9$; (c) $\phi=3\pi/2-2\pi/9$; (d) $\phi=2\pi-2\pi/9$. The Reynolds number for occurrence of these spiral TG vortices Res is 1100 in the numerical simulation. Contour of the zero radial velocity ($u_r=0$) on this section is also drawn with two types of solid lines. Thin solid lines indicate the center positions of the two toroidal TG vortex cells. The thick ones, which are counted by every two thick lines from each side of the equator, correspond to the center lines of the spiral TG vortex.

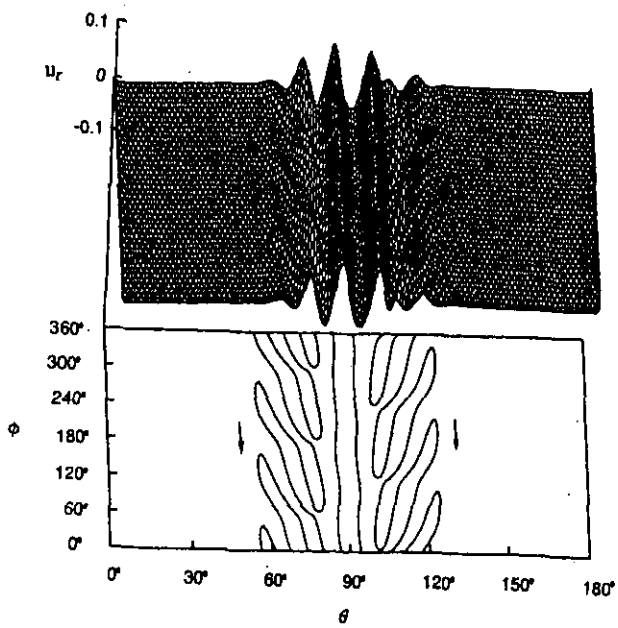

Fig. 2 Bird's-eye view of the radial velocity in the same spherical cross-section as that in Fig. 1 but shown in Cartesian coordinates. For comparison with Fig. 1, the zero contour of the radial velocity (u_r=0) is also projected onto the (θ, ϕ) plane. Arrows show the direction of the spiral TG vortices's movement.

spherical cross-section as that in Fig. 1. To compare it with the same contour line in the Fig. 1, the zero contour of the radial velocity (u_r = 0) is also projected onto the (θ, ϕ) plane. It is observed in Figs. 1 and 2 that there is one toroidal TG vortex and three spiral TG vortices in each hemisphere. The three pairs of the spiral TG vortices are formed on each side of the one pair of the toroidal TG vortices. The lines of the center positions of the toroidal TG vortices(or say the axes of the TG toroidal vortices) are nearly parallel to the equator while the center lines of the spiral TG vortices(or say the axes of the spiral TG vortices) are tilted with respect to the azimuthal direction. Obviously, the spiral TG vortices are equatorially asymmetric and travel in the azimuthal direction(the same as the inner rotating sphere). The arrows in Fig. 2 show the direction of the spiral TG vortices's movement. Table 1 also display the characteristics of the spiral TG vortices simulated with the numerical method and the ones of the experiments (Nakabayashi [8] and Nakabayashi and Tsuchida [9]). Quantitatively, the numerical simulation on the spiral TG vortices gives a good agreement with the experiments.

5. *Summary*

A finite-difference method, which is second-order accurate in time and space, is used to solve three dimensional, time dependent incompressible Navier-

	Toroidal TG Vortex		Spiral TG Vortex	
	Dynamical Characteristics	Geometrical Characteristics	Dynamical Characteristics	Geometrical Characteristics
Experiments	R^*=1 (R_{ec}=900) Steady	Axisymmetric Equal widths to clearance	R^*=1.13 (R_{es}=1017) Move in rotating direction	Three pair of spirals No-equatorial symmetry
Present Study	R^*=1 (R_{ec}=940) Steady	Axisymmetric Equal widths to clearance	R^*=1.18 (R_{es}=1110) Move in rotating direction	Three pair of spirals No-equatorial symmetry

Table 1 Comparison between the numerical simulation and the experimental results.

Stokes equations in spherical polar coordinates. A staggered grid system is considered in the present study, so the treatment of singularities of the equations in spherical polar coordinates is avoided. The discrete velocity equations are solved with the approximate factorization technique and standard TDMA method, while the discrete Poisson equation is solved with the ADI technique and a refined TDMA method. The spherical Couette flow between two concentric spheres with the inner one rotating is computed. We simulated the spiral TG vortex flow, and a comparison of the numerical solutions with the available experimental measurements was also made. It is demonstrated that the three dimensional spiral TG vortex in the spherical Couette flow is well simulated.

Acknowledgments

The computations were carried out with NEC supercomputer(SX4) at the computing center of the National Institute for Environmental Studies, Japan.

References

1. W.Sha, K.Nakabayashi and H.Ueda, J. Comput. Phys. Submitted for publication.
2. J. K. Dukowicz and A. S. Dvinsky, J. Comput. Phys. 102, 336(1992).
3. R. M. Beam and R. F. Warming, J. Comput. Phys. 22, 87(1976).
4. W. R. Briley and H. McDonald, J. Comput. Phys. 24, 372(1977).
5. J. Kim and P. Moin, J. Comput. Phys. 59, 308(1985).
6. D. W. Peaceman and H. H. Rachford, J. Soc. Indust. Appl. Math. 3, 28(1955).
7. C. J. Temperton, J. Comput. Phys. 19, 317(1975).
8. K. Nahabayashi, J. Fluid Mech. 132, 209(1983).
9. K. Nakabayashi and Y. Tsuchida, J. Fluid Mech. 194, 101(1988).
10. K. Nakabayashi and Y. Tsuchida, J. Fluid Mech. 295, 43(1995).
11. G. Dumas and A. Leonard, J. Comput. Phys. 111, 205(1992).